

Magnetic domain engineering in antiferromagnetic CuMnAs and Mn₂Au

Sonka Reimers,^{1,2,3,*} Olena Gomonay,² Oliver J. Amin,¹ Filip Krizek,⁴ Luke X. Barton,¹

Yaryna Lytvynenko^{1,2,5} Stuart F. Poole,¹ Vit Novák^{1,4} Richard P. Campion,¹

Francesco Maccherozzi,³ Gerardina Carbone,⁶ Alexander Björling,⁶ Yuran Niu,⁶ Evangelos Golias,⁶

Dominik Kriegner^{1,2,7} Jairo Sinova,² Mathias Kläui,^{2,8} Martin Jourdan^{1,2,†} Sarnjeet S. Dhesi,³

Kevin W. Edmonds,¹ and Peter Wadley^{1,2}

¹ School of Physics and Astronomy, University of Nottingham, Nottingham NG7 2RD, United Kingdom

² Institut für Physik, Johannes Gutenberg-Universität Mainz, 55099 Mainz, Germany

³ Diamond Light Source, Chilton OX11 0DE, United Kingdom

⁴ Institute of Physics, Czech Academy of Sciences, 162 00 Praha 6, Czech Republic

⁵ Institute of Magnetism of the National Academy of Sciences (NAS) of Ukraine and the Ministry of Education (MES) of Ukraine, 03142 Kyiv, Ukraine

⁶ MAX IV Laboratory, 224 84 Lund, Sweden

⁷ Institute of Solid State and Materials Physics, Technical University Dresden, 01069 Dresden, Germany

⁸ Center for Quantum Spintronics, Norwegian University of Science and Technology (NTNU), 7034 Trondheim, Norway



(Received 17 November 2023; revised 19 February 2024; accepted 17 May 2024; published 12 June 2024)

Antiferromagnetic materials hold potential for use in spintronic devices with fast operation frequencies and field robustness. Despite the rapid progress in proof-of-principle functionality in recent years, there has been a notable lack of understanding of antiferromagnetic domain formation and manipulation, which translates to either incomplete or nonscalable control of the magnetic order. Here, we demonstrate simple and functional ways of influencing the domain structure in CuMnAs and Mn₂Au, two key materials of antiferromagnetic spintronics research, using device patterning and strain engineering. Comparing x-ray microscopy data from two different materials, we reveal the key parameters dictating domain formation in antiferromagnetic devices and show how the nontrivial interaction of magnetostriction, substrate clamping, and edge anisotropy leads to specific equilibrium domain configurations. More specifically, we observe that patterned edges have a significant impact on the magnetic anisotropy and domain structure over long distances and we propose a theoretical model that relates short-range edge anisotropy and long-range magnetoelastic interactions. The principles invoked are of general applicability to the domain formation and engineering in antiferromagnetic thin films at large, which will hopefully pave the way toward realizing truly functional antiferromagnetic devices.

DOI: 10.1103/PhysRevApplied.21.064030

I. INTRODUCTION

Antiferromagnetic (AF) spintronics has the potential to be a breakthrough technology for data storage in terms of speed, scaling, and robustness. Following the theoretical prediction of efficient manipulation of AF order with electrical currents [1], research has focused on proof-of-principle functionality. Thus, rapid progress has been made in this respect both experimentally and theoretically [2–7]. Yet, most cases show incomplete control of the AF order, lack long-term stability, or require large current pulses and significant heating, or even nonscalable approaches, such as the application of large magnetic fields. To overcome

these limitations and realize truly functional devices from antiferromagnets requires an in-depth understanding of antiferromagnetic domain formation and a precise tuning of the local magnetic anisotropy in devices, which to date remains mostly elusive for fully compensated antiferromagnets.

In ferromagnetic devices, domain formation is largely governed by the minimization of magnetic stray fields, which makes the magnetic anisotropy sensitive to the shape of the device [8]. However, magnetic stray fields are entirely absent in the bulk of fully compensated antiferromagnets, so that *a priori* long-range shape-induced phenomena may not be expected.

Nonetheless, it has been reported for devices fabricated from antiferromagnetic oxide films that the domain structure becomes sensitive to the device shape when the

*Corresponding author: sreimers@uni-mainz.de

†Corresponding author: jourdan@uni-mainz.de

dimensions are on the micrometer scale. Studies with LaFeO₃ have revealed both short-range and long-range effects [9–11], with short-range effects related to an edge anisotropy, which leads to a local alignment of the AF spin axes parallel or perpendicular to the lithographic edge. This is mediated only by direct AF exchange over distances up to the typical AF-domain size. Effects over longer ranges have been attributed to magnetoelastic interactions. Also for NiO/Pt heterostructures, it has recently been shown that minimization of elastic energy has a primary role in the domain configuration [12]. In NiO, magnetoelasticity originates from exchange coupling and hence is known to be large.

In the antiferromagnetic metals CuMnAs and Mn₂Au, studied here, magnetoelastic coupling can only arise from the relativistic spin-orbit coupling, which is typically several orders of magnitude smaller than exchange coupling. Nevertheless, as we show in this work, patterned edges also significantly influence the domain structure and magnetic anisotropy in CuMnAs and Mn₂Au thin films. Tetragonal CuMnAs and Mn₂Au are amongst the most promising material candidates for application in AF spintronics, because they are the only materials discovered for which electrical currents can rotate the Néel vector via so-called Néel spin-orbit torques (NSOTs) [2,7,13–15]. Insight into the mechanism of domain formation and anisotropy in these materials is thus directly relevant for AF spintronics research and potential future application.

To understand the effect of patterning on the domain structure, we study the AF domains in simple geometries fabricated from CuMnAs and Mn₂Au films using x-ray magnetic linear dichroism photoemission electron microscopy (XMLD PEEM).

Our experimental data reveal a spatial variation of the local magnetic anisotropy over several micrometers, which we measure as a change of the domain-wall widths in CuMnAs and as a change of the average domain population in the Mn₂Au films. This microscopic investigation of the anisotropy in AF structures gives unique insight into the mechanisms that underpin AF-domain formation and anisotropy changes in patterned structures. We show that the spatial variation of the anisotropy and the characteristic domain structures are directly related to the spatial distribution of strain in the samples, which we model using magnetoelastic charges. We find that short-range edge-induced anisotropy arising at the patterned edges can induce long-range effects due to magnetoelastic interactions competing with the film-substrate clamping. By comparing CuMnAs and Mn₂Au, we disentangle the contributions to the local anisotropy and show how in patterned structures, the same mechanisms result in different stable AF-domain morphologies depending on the material parameters. Our description can be generally applied to domain formation in devices fabricated from epitaxial AF thin films grown on a nonmagnetic substrates, the

most relevant geometry for spintronic application. This study hopefully makes a crucial contribution toward closing the gap between proof-of-principle experiments and truly functional AF-spintronic devices.

A. Samples

Here, we study epitaxial (001)-oriented CuMnAs and Mn₂Au films grown on nonmagnetic substrates. The films have a tetragonal crystal structure and exhibit antiferromagnetic ordering at room temperature, with magnetic moments located on Mn sites. The magnetic moments align ferromagnetically in the (001) plane, with antiferromagnetic coupling between neighboring planes [16, 17]. Both materials exhibit large out-of-plane magnetocrystalline anisotropies, confining the AF spin axis in plane. The in-plane magnetic anisotropies, which are much smaller, favor two mutually orthogonal magnetic easy axes along the <110> crystallographic directions that match the in-plane symmetry of the substrates. Thus, from a magnetoelastic point of view, the samples have the same geometry but the size of the magnetocrystalline anisotropies vary considerably. For Mn₂Au, states with spin alignment along the <110> and <100> crystallographic directions are separated by an energy barrier larger than 1.8 μeV per formula unit (f.u.) [18]. For CuMnAs, experiment and theory indicate near degeneracy of the spin-axis direction in the *a*-*b* plane, with the energy difference between the <110> and <100> crystallographic directions <1 μeV per f.u. close to the resolution limit of the calculation [19] and a preference for the <110> directions (magnetic easy axes hereafter) in 50-nm films as studied here. The out-of-plane anisotropy barrier is far larger in both materials, with 2 meV per f.u. in Mn₂Au [16] and 127 μeV per f.u. in CuMnAs [19].

B. Antiferromagnetic domain imaging

The AF-domain structures are imaged by photoemission electron microscopy (PEEM) with sensitivity to the axis of the Néel vector (AF spin axis hereafter) due to the x-ray magnetic linear dichroism (XMLD) effect. For x-ray polarization along an in-plane high-symmetry crystallographic axis, maximum contrast is achieved between domains aligned parallel and perpendicular to the x-ray polarization direction. The XMLD-PEEM imaging of AF domains has been established for both materials in previous experiments [18,20,21].

II. RESULTS AND DISCUSSION

First, we discuss the patterning-induced AF-domain configurations using CuMnAs as an example and introduce the magnetoelastic model. Later in this paper, we show how this model can be applied to the second investigated antiferromagnet Mn₂Au, which has a much larger magnetocrystalline anisotropy.

The model considers three contributions to the total energy: magnetic energy that contains exchange energy W_{ex} and magnetocrystalline anisotropy W_{mc} , surface energy at the patterned edge, W_{edge} , referred to hereafter as edge energy, and destressing energy at the film-substrate interface, W_{destr} , which is the elastic energy due to magnetostriction of the antiferromagnet and film-substrate clamping. We distinguish between epitaxial (or growth-induced) strain and spontaneous incompatibility strain. The epitaxial strain is isotropic and hence does not break the symmetry between the two magnetic easy axes, and can be neglected in many cases. Only directly at the edge, this strain can be relaxed anisotropically over approximately the distance of the film thickness. This is one possible origin of edge anisotropy. Other contributions to strain relaxation at the edges could originate from local defects generated by the etching procedures, in particular from the ion-beam etching of the Mn₂Au thin films (the CuMnAs samples have been wet chemically etched). However, for our theoretical discussion, the origin of the edge anisotropy is not relevant and, in particular, we show that long-range magnetoelastic interactions act on regions far away from the edges. With the term incompatibility, we refer to the additional spontaneous strain that emerges due to magnetoelastic coupling when comparing the nonmagnetic state with the magnetic state. This is anisotropic and therefore can affect AF-domain formation. Further information can be found in Appendix C.

A. Effect of patterning in CuMnAs

High-quality epitaxial CuMnAs films, of 50-nm thickness, are grown by molecular-beam epitaxy or GaP(001) substrates, with a mismatch between film and substrate of approximately 0.3 %. The films are grown fully strained. Epitaxial strain is relaxed locally in the vicinity of specific crystallographic nanoscale defects, referred to as microtwins [22]. Nonpatterned (as-grown) samples of the films studied here consist of two types of AF domains with mutually orthogonal spin axes, along the ⟨110⟩ crystallographic directions of the films. Previous work has shown that the domain morphology and size are governed by nanoscale microtwin defects [23]. The microtwins terminate at the surface as characteristic lines along the crystallographic ⟨110⟩ directions and locally pin the AF spin axis parallel to their direction. The strain field surrounding such a twin defect can stabilize 180° domain walls due to magnetostriction [23]. For the sake of simplicity, we will refer to the ⟨110⟩ directions as the magnetic easy axis and the ⟨100⟩ directions as the magnetic hard axis, for these films.

Structures with different geometric shapes are fabricated using photolithography and chemical wet etching from a layer with low microtwin density and typical domain sizes beyond 10 μm². A representative example of the domain structure in a nonpatterned area is shown in Fig. 1(a).

We first consider the simplest device geometry consisting of bars oriented along a magnetic easy axis. In Fig. 1, we compare the AF-domain structures in bars of different widths [Figs. 1(b)–1(g)] to the domain structure in a nonpatterned area [Fig. 1(a)]. A strong effect of the patterning on the AF-domain population and morphology is observed. In a nonpatterned area, the population of orthogonal domain types is almost equal, whereas in the bars, the AF spin axis is aligned mostly parallel to the long edge: the horizontal bars [Figs. 1(e) and 1(g)] show a prevailing presence of horizontal spin axis (light areas), whereas the vertical bars [Figs. 1(b)–1(d)] appear mostly dark. Domains with an orthogonal spin axis are observed only as characteristic lens-shaped domains aligned perpendicular to the edges. Direct comparison to scanning x-ray diffraction microscopy (SXDM) images of the microtwin structure [Figs. 1(f) and 1(h)] show that each lens-shaped domain corresponds to a microtwin defect, which is located at the center of the lens-shaped domain. Microtwin-free areas are fully aligned parallel to the edge of the bar. We have observed the stabilization of the AF spin axis parallel to the edge across the entire widths of the bar, even in the largest 25-μm-wide structures.

In addition to the lens-shaped domains, 180° domain walls are observed. These 180° domain walls are characteristic for uniaxial anisotropy. They appear as narrow undulating lines in the XMLD-PEEM images and often run parallel to the long side of the bar. However, when terminating at an edge, they locally align perpendicular to the edge, similar to what has been observed for 180° domain walls at the surfaces of uniaxial Cr₂O₃ single crystals [24]. This happens at positions sufficiently far away from microtwin defects so that their influence can be neglected.

In the case of patterned edges along a magnetic hard axis (Fig. 2), the XMLD-PEEM images reveal that the AF spin axis aligns *perpendicular* to the edge. This is opposite to what has been observed for edges aligned with the magnetic easy axes. Thus, the patterning-induced anisotropy exceeds the intrinsic magnetocrystalline anisotropy of CuMnAs. In the vicinity of microtwin defects, e.g., at the right corner of the device in Figs. 1(a) and 1(b), the competition of the effect of microtwins and the patterned edge leads to a frustrated domain structure.

To describe domain formation in CuMnAs theoretically, we consider the case of a large edge anisotropy and large exchange energy compared to the destressing energy. In this scenario, the AF spin axis is fixed at the edges. As exchange energy dominates over destressing energy, the entire bar can end up in a single domain state dictated by the edge anisotropy. This is parallel to the bar for edges along a magnetic easy axis and perpendicular for edges along a magnetic hard axis. This kind of dependence of the sign of the edge anisotropy on the patterning direction has also been observed in LFO (see Ref. [9]). It clearly shows that in antiferromagnets, edge anisotropy does not

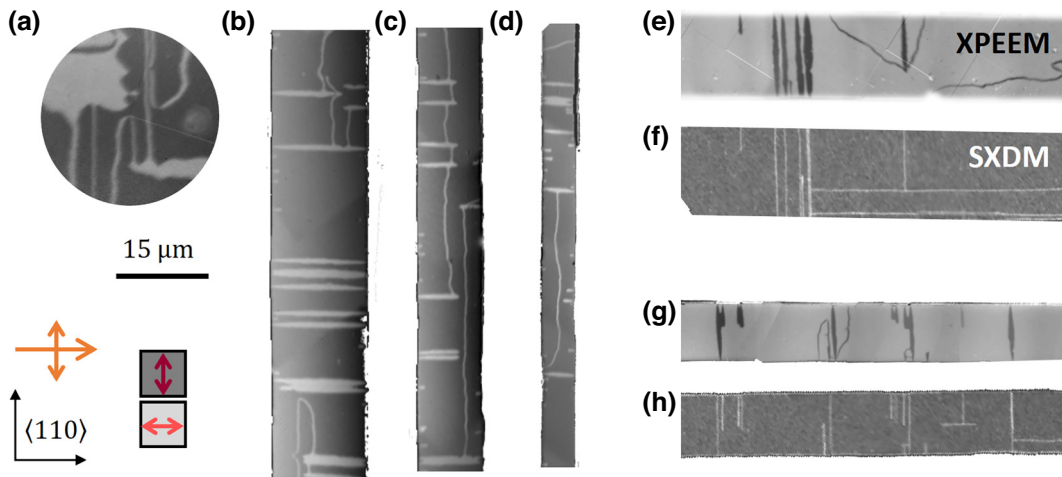


FIG. 1. The effect of patterning along a magnetic easy axis in CuMnAs. (a) AF domains in a nonpatterned area imaged by XMCD PEEM. The orange arrows show the direction and polarization of the incident x-ray beam, which yields sensitivity to the spin axis as shown by the red double-headed arrows. (b)–(d) AF-domain images in (b) 15- μm -, (c) 10- μm -, and (d) 5- μm -wide bars along an easy axis. (e) An AF-domain image of a 15- μm -wide bar with orthogonal orientation. (f) A scanning x-ray diffraction microscopy (SXDM) image of the same bar showing the microtwin configuration. (g),(h) The same as (e) and (f) but for a 10- μm -wide bar.

arise from the minimization of small magnetic stray fields but can have different origins. It can arise from, e.g., the different chemical environment of the surface atoms (e.g., oxidation) or from strain relaxation.

For further insight into the mechanism, we study the spatial variation of the anisotropy, in particular its dependence on the distance to the patterned edges. The widths of 180° domain walls (DWs) act as a local probe of the magnetic anisotropy, since they scale as $1/\sqrt{K}$ with the anisotropy constant K [25]. Two representative examples of domain walls that terminate at edges are shown in Figs. 3(a) and 3(b). Upon close inspection, it can be seen

that the domain walls are considerably narrower in the direct vicinity of the edge. This can be clearly seen in a plot of the domain-wall widths as a function of the distance to the edge [Fig. 3(c)]. The data show that the change occurs continuously over several micrometers. The domain-wall widths reduce to almost half their value (approximately 120 nm) in the vicinity of the edges compared to the center of the bars (200–250 nm). Even in the center, they remain below the widths measured in nonpatterned areas of approximately 260 nm in this sample (shown by the dotted line).

This shows that the anisotropy is not just altered directly at the edge but over long ranges. To understand this long-range effect, the elastic effect of the alignment of the AF spin axis needs to be considered: the alignment of the spin axis with the edge leads to a deformation of the film. This, vice versa, creates a preference for AF domains aligned accordingly, i.e., an additional uniaxial anisotropy and can explain, e.g., the presence of 180° domain walls even in biaxial magnetic systems [25]. Yet, the corresponding lattice deformation of the film is incompatible with the nondeformed substrate.

Mathematically, we model this incompatibility with an elastic charge density at the film-substrate interface, illustrated by the purple sheet in Fig. 3(d). A single domain configuration corresponds to a uniform charge density. This charge density creates a long-range “Coulomb-like” elastic field in film and substrate, similar to the electric field of a uniformly charged finite plate. It is largest in the center of the bar and counteracts the patterning induced effect. Hence the anisotropy is largest at the edge and reduces toward the center of the bar. This translates into a characteristic dependence of the domain-wall widths as a

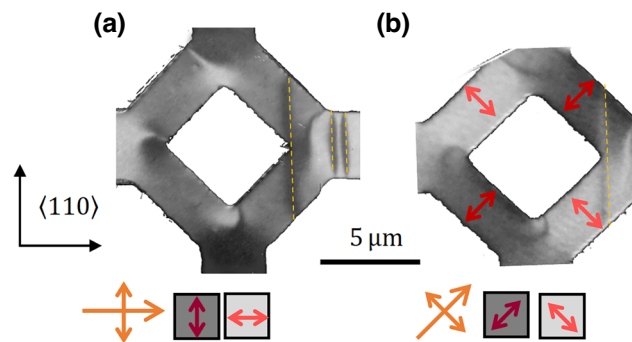


FIG. 2. The effect of patterning along a magnetic hard axis in CuMnAs. (a) AF domains in a square-shaped almost microtwin-free device imaged with x-ray polarization along a CuMnAs $\langle 110 \rangle$ direction, as indicated by the double-headed orange arrows. The yellow dashed lines mark the positions of microtwin defects. (b) The same device, but imaged with x-ray polarization along a CuMnAs $\langle 100 \rangle$ direction, which reveals that the AF spin axis aligns perpendicular to the edge.

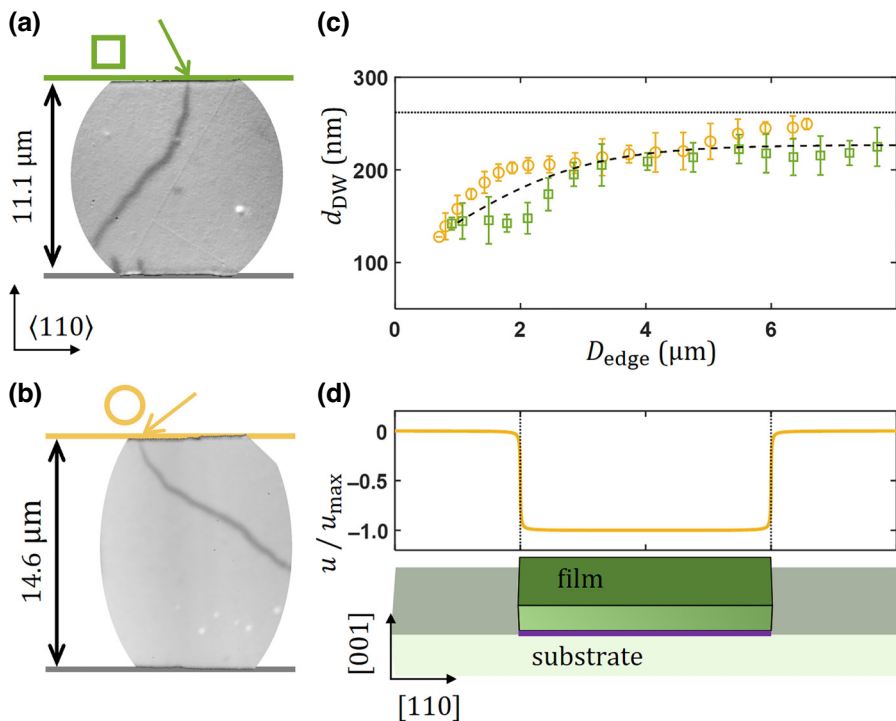


FIG. 3. The gradient anisotropy in CuMnAs bars. (a),(b) 180° DWs in a CuMnAs bar. (c) The dependence of the widths of the DWs in (a) and (b) on the distance to the edge, measured with respect to the colored edge. The green and yellow data points correspond to the images in (a) and (b). The dashed line shows the simulated dependence of the DW width. The dotted line shows the DW width measured in nonpatterned areas of the sample. (d) A schematic illustrating the origin of the effect. The purple sheet displays the magnetoelectric charge density causing the destressing field u shown in the inset (yellow curve). This field opposes the single-domain state and reduces the anisotropy toward the center of the bar.

function of distance to the edge (see Appendix C), shown by the dashed line in Fig. 3(c), which is an averaged fit of the data sets. The good agreement of the model with the experimental data supports the validity of our theoretical description. Deviations of the data from the theoretical curve can be ascribed to local crystallographic defects.

We have shown that the AF-domain formation is governed by the competition of edge anisotropy, exchange, and destressing energy. In the CuMnAs structures, the destressing energy is small and the final state is largely governed by edge anisotropy and exchange energy. The effect of the destressing energy manifests itself as the broadening of the domain walls toward the center of the bars. The competition between the edge anisotropy and the destressing field becomes more obvious in the Mn₂Au films studied and discussed next.

B. Patterning effects in Mn₂Au

The (001)-oriented Mn₂Au films are 40 nm thick and are grown epitaxially on Ta(001)/Mo(001) double buffer layers on MgO(001) substrates [14]. As mentioned above, Mn₂Au, like CuMnAs, has two mutually orthogonal equivalent magnetic easy axes but a much larger magnetocrystalline anisotropy. Both magnetocrystalline anisotropy and magnetoelasticity originate from

spin-orbit interaction, which is larger in Mn₂Au due to its heavier mass, and therefore magnetoelasticity can also be expected to be considerably larger in Mn₂Au than in CuMnAs, so that the destressing energy becomes more relevant.

Without patterning, the epitaxial Mn₂Au thin films show a multidomain AF-domain state, with two types of domains aligned with the two magnetic easy axes and equipartititl distribution of the two domain types. A representative example is shown in Fig. 4(a). The domain size is in the order of 1 μm, considerably smaller compared to the CuMnAs samples discussed above. Consistent with our assumption, a smaller domain size is expected for systems in which the destressing energy is more relevant. No evidence of morphological structures or crystallographic defects on the same length scale as the magnetic domains has been found. The width of the domain walls in Mn₂Au is less than 80 nm, close to the resolution limit of the XMLD-PEEM technique, much smaller than in CuMnAs, where the domain-wall widths can vary significantly depending on the local defect structure [23]. This shows the more than 30 times larger magnetocrystalline anisotropy of Mn₂Au, which is obtained by additionally considering the about 4 times higher Néel temperature of Mn₂Au [26].

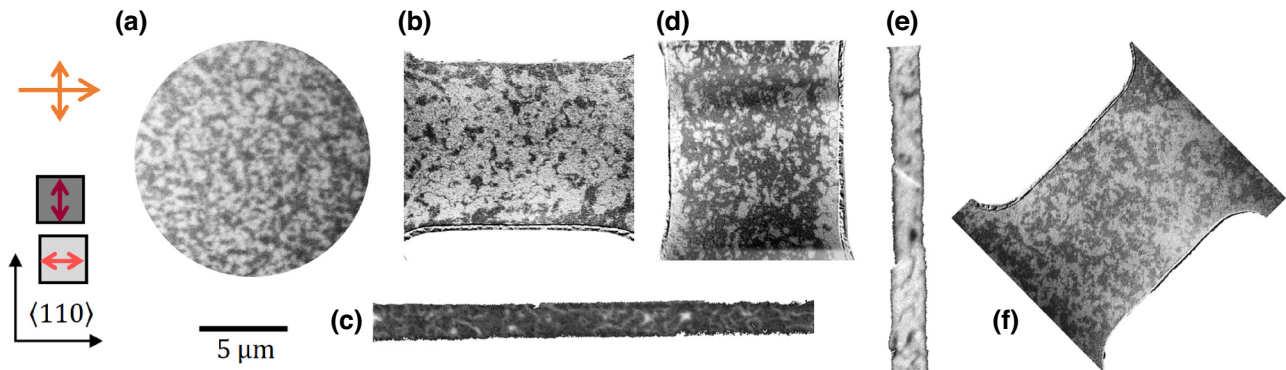


FIG. 4. The effect of patterning in Mn_2Au . (a) A nonpatterned area. (b),(c) In a (b) 10- μm -wide and a (c) 2- μm -wide bar along the magnetic easy axes. (d),(e) Same as (b) and (c) but for bars with orthogonal orientation. (f) AF domains in a 10- μm -wide bar along a magnetic hard axis. The orange arrows show the direction and polarization of the incident x-ray beam.

To study the effect of patterning on this type of domain structure, devices with similar bar geometries are fabricated using photolithography and Ar^+ ion-beam milling. In Fig. 4, we compare the AF-domain structure in patterned bars with different orientations to the nonpatterned case.

As in the case of CuMnAs, the bars oriented along magnetic easy axes [Figs. 4(b)–4(e)] show a pronounced effect of the microlithography on the AF-domain structure. However, in contrast to CuMnAs, the competing effects of the edge anisotropy and the destressing field can be observed directly: in the 10- μm -wide bars [Figs. 4(b)], the AF spin axis is aligned perpendicular to the edge in a narrow approximately 0.5–1.0- μm near-edge region. This orientation is stabilized across the entire bar, if the width of the bar approaches the typical domain size, as in the narrow 2- μm -wide bars [Figs. 4(c) and 4(e)]. In these, only one type of domain and 180° domain walls are observed. In the wider bars away from the near-edge region, domains with their AF spin axis along both perpendicular easy axes are observed but domains with AF spin axis parallel to the edges clearly dominate the domain population. This indicates that the effects of the destressing field are dominant.

In Fig. 4(f), we show the AF domains in a bar patterned along a magnetic hard axis. In this device, no effect of the patterning on the domain structure can be observed. The only detectable variation compared to nonpatterned areas occurs in the corners of the device, i.e., where the edge is locally aligned with a magnetic easy axis. Hence, in Mn_2Au , the edge anisotropy is not sufficiently strong to overcome the intrinsic anisotropy and cannot force the AF spin axis onto a hard axis of the magnetocrystalline anisotropy.

Mn_2Au is an example where the magnetocrystalline anisotropy and the destressing energy are relatively large. Consequently, as-grown unpatterned samples show a multidomain state with equi-partitital population of the two

domain types, which minimizes destressing energy and patterning-induced anisotropy cannot fully rotate the AF spin axis but only affects the relative population of the domains. Thus, patterned edges along a magnetic hard axis have no measurable effect of the AF-domain structure. In narrow (2- μm) bars along the magnetic easy axis, the AF spin axis is almost fully aligned perpendicular to the edge, which can be explained by the edge anisotropy and direct exchange alone; the 180° domain walls are of kinetic origin. However, as the destressing energy is larger than in CuMnAs, this alignment is not maintained over the complete width of the wider (10- μm) bars. In these wider bars, the AF-domain population in the center of the bars is reversed compared to the near-edge region. The variation of the domain population as a function of the distance to the edge is shown in Fig. 5. The nonequipartitital distribution of domains is observed across the entire width of the bars, which exceed the typical AF-domain size by an order of magnitude. This is clear evidence for an elastic origin of the effect and can be described within our model as follows.

The alignment of the AF spin axis of the near-edge region due to edge anisotropy deforms the lattice of the film, so that the average strain is nonzero at the edges and creates additional strain due to incompatibility (modeled as magnetoelastic charges of one sign). This increases the destressing energy compared to a state with zero average strain. Hence, Mn_2Au reacts by creating domains with an orthogonal spin axis (charges of opposite sign). Mathematically, we can model the incompatibility with a magnetoelastic charge density at the interface. The sign and size of the charge density are proportional to the ratio of the two domain types; hence the center and the boundary layer have opposite sign. We then start with an initial guess of the distribution of the domains, calculate the charge density and corresponding energy, and iteratively approach a state that minimizes the energy, corresponding to a stable

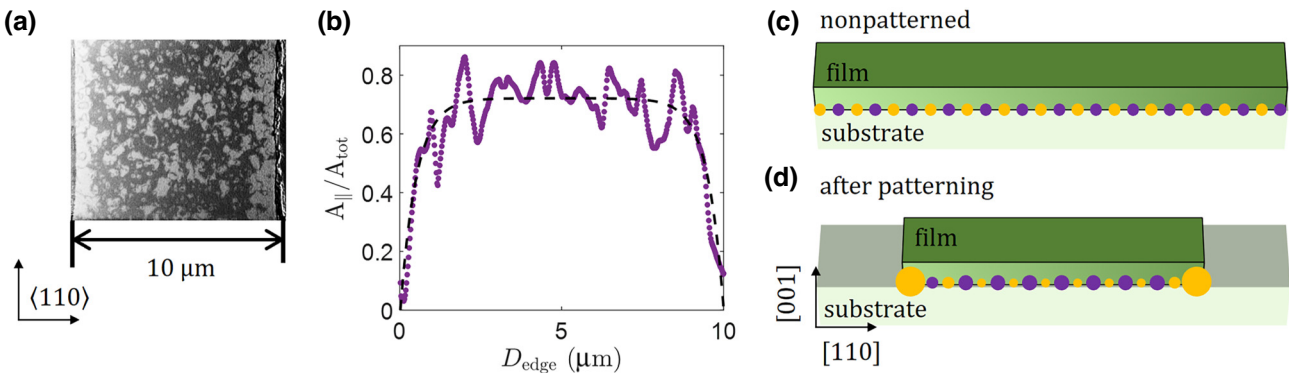


FIG. 5. Gradient anisotropy in Mn₂Au bars. (a) AF domains in a 10-μm-wide Mn₂Au bar. (b) The average domain population as a function of the distance to the left edge. The purple dots are experimental data and the black dashed line is a theoretical simulation. (c) The magnetoelastic charge configuration before patterning: purple and yellow correspond to opposite charge. (d) The magnetoelastic charge configuration after patterning. Edge anisotropy imposes alignment of the AF spin axis at the edges, creating an imbalance of charges. This increases the destressing energy, so that the film reacts by the expansion of domains with opposite charge in the center.

AF-domain configuration. Consistent with experiment, the model predicts a sharp rise of the domain population over a short distance and almost a plateau in the central area, in good agreement with the experimental data.

C. Relevance for current induced switching experiments

CuMnAs and Mn₂Au are two of the most important conducting materials for AF spintronics. Most experimental and theoretical studies with these materials are concerned with the manipulation of their AF order via NSOTs. Yet, the behavior of the AF-domain structure is directly related to the AF anisotropy and the equilibrium domain structure, as well as several potential metastable states. As we show here, these depend on the shape of the device. Thus, our findings are of great relevance for the interpretation of previous work on AF-domain manipulation and can be used to optimize devices for future experiments.

Our data show that there is an equilibrium domain configuration in patterned structures, i.e., in potential AF spintronics devices, which is different from the as-grown state. In the context of switching between two orthogonal orientations of the Néel vector, as originally proposed for AF magnetic random access memory (MRAM), this raises the question of whether the switched states can be stable in the long term and if the AF-domain structure relaxes to the equilibrium configuration by thermal activation. Here, we note two things: first, in CuMnAs, neither electrical current pulses nor magnetic fields have been able to induce long-term stable switching by 90° of a large fraction of the active area of a device at room temperature. On the contrary, the switching is characterized by significant decay [27–29]. This can be understood by considering the existence of a ground state that is dictated by patterning in combination with the low magnetocrystalline anisotropy. Second, for Mn₂Au, long-term stable

switching of a large area of a device at room temperature has been demonstrated and no relaxation of electrical switching at room temperature is observed [14]. This is because the domain walls in this material are narrower and more strongly pinned. The lack of relaxation at room temperature is consistent with the fact that the AF-domain structure is altered during the patterning process, because the Ar⁺ ion-beam milling used significantly heats the sample. This helps to overcome the domain-wall pinning barriers required to achieve the new equilibrium configuration, whereas at room temperature, the pinning barriers are sufficiently large to prevent relaxation of the current-induced metastable state. This example illustrates that applications rely on a fine tuning of the anisotropy and that knowledge of the effect of patterning is crucial in order to design suitable device geometries. For example, for applications that rely on orthogonal switching of the Néel vector between two magnetic easy axes, edges along the magnetic easy axes lead to significant pinning, thus limiting the device efficiency. Consistently, in Ref. [14], long-term stable and reversible switching of effectively the entire active area of a Mn₂Au device has been shown with an “easy-edge-free” device geometry. Recent work has also suggested applications beyond AF MRAM, including novel computing based on complex AF textures such as vortices and AF merons [30]. Of the two materials studied there, these are most likely to be realizable in CuMnAs devices with low magnetocrystalline anisotropy, in which the competition of the edge effect and microtwin defects can be used to engineer a frustrated anisotropy landscape. This can be achieved by patterning edges along the magnetic hard axis. Indeed, such a geometry has been used in Ref. [31], where AF merons have been electrically generated. In contrast, an enhanced uniaxial anisotropy might be beneficial for devices based on the motion of 180° domain walls, as could be envisioned for an AF racetrack memory.

III. CONCLUSIONS

Microlithography has been shown to have a significant impact on the AF domains and magnetic anisotropy in both CuMnAs and Mn₂Au films. When edges are patterned, an additional anisotropy is induced, which results in a preferred alignment of the AF spin axis. This patterning-induced anisotropy can surpass the bulk magnetocrystalline anisotropy in materials such as CuMnAs, where the intrinsic anisotropy is small. However, even in materials with larger intrinsic anisotropy, such as Mn₂Au, the patterning-induced anisotropy has a significant impact on the AF-domain structure. In devices, this leads to pronounced gradients of the anisotropy that can be directly measured as a change of 180° domain-wall widths in CuMnAs or inferred from the average domain population in Mn₂Au. Patterned edges, which are inevitable in devices, can therefore be utilized as a tool to tune the anisotropy and domain structure for both applications and experiments involving these widely investigated materials. By comparing data from both materials, a model of domain formation in AF devices has been developed, which allows for the disentanglement of the different contributions that govern the AF-domain structure and the local magnetic anisotropy. For instance, the anisotropy gradients are shown to be governed by the spatial distribution of strain. The model establishes a relationship between short-range edge anisotropy and long-range magnetostrictive effects via magnetoelastic charges, in analogy to electrostatics. The principles of edge anisotropy, magnetostriction, and anisotropic strain relaxation at patterned edges are generic to all antiferromagnetic films grown on nonmagnetic substrates. Therefore, the model is generally applicable to antiferromagnetic devices. The understanding of the mechanisms that govern domain formation and the local anisotropy in such structures forms the basis to precisely tune them toward specific applications. This will hopefully facilitate the realization of functional and efficient spintronic devices.

ACKNOWLEDGMENTS

We thank Diamond Light Source for the allocation of beam time on beam line I06 under Proposals No. MM22437-1 and No. NT27146-1. We acknowledge the MAX IV Laboratory for beam time on the NanoMAX beam line under Proposal No. 20190533 and for time on the MAXPEEM beam line under Proposal No. 20210863. Research conducted at MAX IV, a Swedish national user facility, is supported by the Swedish Research Council under Contract No. 2018-07152, the Swedish Governmental Agency for Innovation Systems under Contract No. 2018-04969, and Formas under Contract No. 2019-02496. S.R. acknowledges support from Diamond Light Source Studentship Grant No. STU0201. S.R., M.J., and M.K. acknowledge financial support by the Horizon 2020

framework program of the European Commission under FET-Open Grant No. 863155 (s-Nebula) and funding by the Deutsche Forschungsgemeinschaft (DFG, German Research Foundation) Grant No. TRR173/2—268565370 Spin-X (Projects A01 and A05). O.G. and J.S. acknowledge the Deutsche Forschungsgemeinschaft via Grant No. TRR 288–422213477 (project A09) and via Grant No. TRR 173/2—268565370 (projects A03 and B12). J.S. additionally acknowledges funding from Grant Agency of the Czech Republic via Grant No. 19-28375X. V.N. and F.K. acknowledge financial support from the Czech Ministry of Education Grants No. LM2023051 and LNSMLNSpin, and Czech Science Foundation via Grant No. 19-28375X. D.K. acknowledges the Lumina Quaeruntur fellowship LQ100102201 of the Czech Academy of Sciences and Grant No. 22-22000M from the Czech Science Foundation.

APPENDIX A: SAMPLE-PREPARATION METHODS

1. Material growth

The 50-nm CuMnAs(001) films were grown by molecular-beam epitaxy on a GaP buffer layer on GaP(001) substrates at 210 °C. The films were capped with a 3-nm Al layer to prevent surface oxidation. Details of the MBE growth can be found in Ref. [22]. *Ex situ* x-ray diffraction (XRD) diffraction measurements confirmed the tetragonal crystal structure of the layer, with the epitaxial relationship CuMnAs(001)[100]||GaP(001)[110]. XRD measurements and scanning transmission electron microscopy (STEM) suggest that the films are grown fully strained, with epitaxial strain relaxed only in the vicinity of specific crystallographic nanoscale defects, referred to as microtwins [22].

The 40-nm Mn₂Au(001) films were prepared by radio-frequency magnetron sputtering (rf sputtering). The Mn₂Au(001) films were deposited on MgO(001) substrates with 20-nm Mo(001) and 16-nm Ta(001) double buffer layers and capped with 2-nm Si₃N₄. The Mn₂Au layers were deposited at approximately 500 °C and subsequently annealed for 75 min at 700 °C. For further information, see Ref. [32]. The tetragonal structure and crystalline quality of the films was confirmed with *ex situ* x-ray diffraction, establishing the Mn₂Au(001)[100]||MgO(001)[110] epitaxial relationship.

In the main text, the crystallographic axes always refer to the CuMnAs/Mn₂Au films and not to the substrates.

2. Device fabrication

The CuMnAs devices were fabricated by optical lithography and chemical wet etching.

The Mn₂Au devices were fabricated by optical lithography and Ar⁺ ion-beam milling with a continuous Ar⁺

current, which is associated with sample heating up to ≈ 150 °C. The etching process removes the entire Mn₂Au and buffer layers and part of the substrate.

APPENDIX B: IMAGING METHODS

1. XMLD-PEEM imaging

The XMLD-PEEM measurements were performed on beam line I06 at Diamond Light Source and at the MAX-PEEM beam line at MAX IV. On I06 at Diamond, the x-ray beam was incident at a grazing angle, forming an angle of 16.5° with the sample surface. Magnetic contrast was obtained from the difference in the absorption signal measured by XPEEM at the peak and the minimum of the Mn L_{2,3} XMLD spectrum. At the MAXPEEM beam line, the x-ray beam has normal incidence on the sample surface. Magnetic contrast was obtained from the difference of the absorption measured by XPEEM for two mutually perpendicular in-plane polarizations for a fixed photon energy at the maximum of the Mn L_{2,3} XMLD spectrum. The different measurement configurations only affect the absolute scale of the signal and thus are irrelevant after image normalization.

All measurements were performed at room temperature and with approximately 50-nm spatial resolution.

The dependencies of the XMLD on the crystal orientation of CuMnAs have been determined previously using an exchange-coupled Fe/CuMnAs bilayer [20]. It has been shown that the XMLD spectrum has a similar shape but opposite sign for $\vec{E}||[100]$ and $\vec{E}||[110]$. For Mn₂Au, the dependence of the XMLD for $\vec{E}||[110]$ has been established from Mn₂Au samples that have been exposed to an in-plane 30-T magnetic field. This induces a spin-flop transition and leads to approximately 80 % remanent AF spin-axis orientation perpendicular to the field [26,33].

On beam line I06, images were acquired with a LEEM III microscope operated at 12 keV for the CuMnAs samples and at 15 keV for the Mn₂Au samples. On the MAX-PEEM beam line at MAX IV, the LEEM III microscope was operated at 20 keV.

2. Scanning x-ray diffraction microscopy (SXDM)

SXDM imaging of microtwin patterns in CuMnAs devices was performed at the NanoMAX beam line at the MAX IV Laboratory. The x-ray beam with an energy of 10 keV was focused to a lateral diameter of 100 nm onto the sample onto the sample, aligned to satisfy a Bragg condition, and rastered across the sample surface in a two-dimensional mesh at different angles around the Bragg peak. The three-dimensional reciprocal space maps thus obtained provided information about structural features of the sample (see Ref. [23]) and rastered across the sample surface in an x-y mesh during a scan. As discussed in Ref. [23], the microtwins create specific features (wings) at

Bragg-reflection peaks. This allows to map the microtwin configuration by plotting the intensity measured on the wings against the sample position during a scan. These intensity maps were obtained at the CuMnAs(003) peak of the sample at an angle $\Delta\Theta = \pm 0.4$ ° from the Bragg angle, i.e., $\Theta = \Theta_{\text{Bragg}} \pm \Delta\Theta$ and the x-ray beam impinging along the CuMnAs [110] direction for $\Theta = \Theta_{\text{Bragg}}$ (for further details, see Ref. [23]).

APPENDIX C: FITTING PROCEDURES

1. Measuring the widths of 180° domain walls

The image processing and data fitting was done using MATLAB R2018b.

To measure the width of the 180° domain walls, intensity profiles of line cuts across the walls in the XMLD-PEEM images were extracted and a phenomenological model was fitted to the data. For simplicity, the in-plane anisotropy is modeled with a single phenomenological uniaxial term (anisotropy constant K). The out-of-plane anisotropy is assumed to be strong enough to keep the Néel vector in plane. In this case, orientation of the Néel vector is parametrized with a single angular variable φ calculated from the easy-axis direction: $\mathbf{n} = (\cos \varphi, \sin \varphi, 0)$. The domain-wall profile is then given by a standard expression,

$$\varphi - \varphi_\infty = \arccos \left[-\tanh \left(\frac{x - x_0}{d_{\text{DW}}} \right) \right], \quad (\text{C1})$$

where $\varphi_\infty = 0$ or π describes the Néel vector orientation for $x \rightarrow -\infty$, x_0 is the position of the center of the domain wall, and $d_{\text{DW}} = \sqrt{A/K}$ is the characteristic length scale of the rotation, the “domain-wall widths,” defined by the ratio of the exchange stiffness and anisotropy constants A and K . Taking into account the functional form of the XMLD effect, one obtains for x-ray polarization along a CuMnAs [110] direction,

$$\text{MLD}_{[110]} = A_0 \cdot \left[\tanh \left(\frac{x - x_0}{d_{\text{DW}}} \right) \right]^2 + C, \quad (\text{C2})$$

where A_0 and C are constants that depend on the size of the XMLD signal and on the image normalization.

To ensure that the profile was obtained in the direction perpendicular to the domain wall, for each point on the domain wall, the angle of the profile was varied, the profiles fitted, with fitting parameters d_{DW} , x_0 , A_0 , and C , and the minimal d_{DW} chosen.

A detailed description of the fitting protocols is given in the Supplemental Material [34].

2. Modeling elastic incompatibility

For modeling the effect of the elastic incompatibility, we use the formalism developed in Refs. [12,35]. The

distribution of the Néel vector at the interface with the nonmagnetic substrate is treated as a source of incompatibility charges that create the additional strain u^{elas} both in the antiferromagnetic and the nonmagnetic layers.

3. Domain-wall width in CuMnAs stripes

In the presence of additional strain, the domain-wall width $d_{\text{DW}} = \sqrt{A/K_{\text{eff}}}$ depends on the effective anisotropy $K + H_{\text{me}}M_s(u_{xx}^{\text{elas}} - u_{yy}^{\text{elas}})$, where H_{me} is the parameter of magnetoelastic coupling and $M_s/2$ is the sublattice magnetization.

For a given distribution of the Néel vector, the additional strain is calculated as [35]

$$u_{xx}^{\text{elas}}(\mathbf{r}) = -u_{yy}^{\text{elas}}(\mathbf{r}) = \frac{u_{\text{spon}}}{4\pi} \int d\mathbf{r}' \frac{\cos 2\varphi(\mathbf{r}')}{|\mathbf{r} - \mathbf{r}'|} \delta'(z'), \quad (\text{C3})$$

where u_{spon} is the value of the spontaneous strain. We have used Eq. (C3) to calculate the strain distribution within the CuMnAs stripe, assuming a single-domain state $\varphi = 0$ within a stripe region. The calculated function $u_{xx}^{\text{elas}} - u_{yy}^{\text{elas}}$ is then substituted into the expression for the domain-wall width d_{DW} . We obtain

$$\frac{1}{d_{\text{DW}}^2} = \frac{1}{D^2} (1 - ae^{-x/el}), \quad (\text{C4})$$

where x is the distance from the edge and a , D , and el are phenomenological parameters. D can be interpreted as the domain-wall widths at infinity and el as the length scale of the problem. To fit the experimental data with the theoretical curve, we compare the calculated and experimental dependencies $1/d_{\text{DW}}^2$ as a function of distance from the stripe edge by fitting Eq. (C4) to the experimental data. We obtain $D = 227(8)$ nm and $el = 1.1(2)$ μm .

4. Domain distribution in Mn₂Au stripes

The equilibrium distribution of the Néel vector taking into account incompatibility effects can be calculated by minimization of the destressing energy [35]:

$$W_{\text{dest}} = \frac{1}{2} H_{\text{me}} M_s u_{\text{spon}} \int d\mathbf{r} \int d\mathbf{r}' \frac{\cos 2[\varphi(\mathbf{r}') - \varphi(\mathbf{r})]}{|\mathbf{r} - \mathbf{r}'|} \delta'(z'). \quad (\text{C5})$$

For the calculation of the domain distribution in Mn₂Au we use a multiscale approach (see, e.g., Refs. [36,37]). We distinguish two principal scales: the large one defined by the stripe (sample) size and an intermediate one, which is much larger than the domain size but much smaller than the sample size. After averaging over the smaller scale $\langle \cos 2\varphi(\mathbf{r}) \rangle = 2\xi(\mathbf{r}) - 1$, where $\xi(\mathbf{r})$ is the fraction of the

domains with $\varphi = 0$ and $\langle \sin 2\varphi(\mathbf{r}) \rangle = 0$, we minimize the destressing energy,

$$W_{\text{dest}} = \frac{1}{2} H_{\text{me}} M_s u_{\text{spon}} \int d\mathbf{r} \int d\mathbf{r}' \times \frac{(2\xi(x) - 1)(2\xi(x') - 1)}{|\mathbf{r} - \mathbf{r}'|} \delta'(z'), \quad (\text{C6})$$

assuming that $\xi(x) = 1$ at the stripe edges (due to the edge anisotropy).

- [1] J. Železný, H. Gao, K. Výborný, J. Zemen, J. Másek, A. Manchon, J. Wunderlich, J. Sinova, and T. Jungwirth, Relativistic Néel-order fields induced by electrical current in antiferromagnets, *Phys. Rev. Lett.* **113**, 157201 (2014).
- [2] P. Wadley *et al.*, Electrical switching of an antiferromagnet, *Science* **351**, 587 (2016).
- [3] T. Kosub, M. Kopte, R. Hühne, P. Appel, B. Shields, P. Maletinsky, R. Hübner, M. O. Liedke, J. Fassbender, O. G. Schmidt, and D. Makarov, Purely antiferromagnetic magnetoelectric random access memory, *Nat. Commun.* **8**, 13985 (2017).
- [4] D. Xiong, Y. Jiang, K. Shi, A. Du, Y. Yao, Z. Guo, D. Zhu, K. Cao, S. Peng, W. Cai, D. Zhu, and W. Zhao, Antiferromagnetic spintronics: An overview and outlook, *Fundam. Res.* **2**, 522 (2022).
- [5] X. Chen, T. Higo, K. Tanaka, T. Nomoto, H. Tsai, H. Iizuchi, M. Shiga, S. Sakamoto, R. Ando, H. Kosaki, T. Matsuo, D. Nishio-Hamane, R. Arita, S. Miwa, and S. Nakatsuji, Octupole-driven magnetoresistance in an antiferromagnetic tunnel junction, *Nature* **613**, 490 (2023).
- [6] P. Qin, H. Yan, X. Wang, H. Chen, Z. Meng, J. Dong, M. Zhu, J. Cai, Z. Feng, X. Zhou, L. Liu, T. Zhang, Z. Zeng, J. Zhang, C. Jiang, and Z. Liu, Room-temperature magnetoresistance in an all-antiferromagnetic tunnel junction, *Nature* **613**, 485 (2023).
- [7] P. Wadley, S. Reimers, M. J. Grzybowski, C. Andrews, M. Wang, J. S. Chauhan, B. L. Gallagher, R. P. Campion, K. W. Edmonds, S. S. Dhesi, F. Maccherozzi, V. Novak, J. Wunderlich, and T. Jungwirth, Current polarity-dependent manipulation of antiferromagnetic domains, *Nat. Nanotechnol.* **13**, 362 (2018).
- [8] C. Kittel, Physical theory of ferromagnetic domains, *Rev. Mod. Phys.* **21**, 541 (1949).
- [9] A. D. Bang, I. Hallsteinisen, R. V. Chopdekar, F. K. Olsen, S. D. Sløetjes, K. Kjærnes, E. Arenholz, E. Folven, and J. K. Grepstad, Shape-imposed anisotropy in antiferromagnetic complex oxide nanostructures, *Appl. Phys. Lett.* **115**, 112403 (2019).
- [10] E. Folven, T. Tybell, A. Scholl, A. T. Young, S. T. Retterer, Y. Takamura, and J. K. Grepstad, X-PEEM study of antiferromagnetic domain patterns in LaFeO₃ thin films and embedded nanostructures, *Nano Lett.* **10**, 4578 (2010).
- [11] E. Folven, Y. Takamura, and J. K. Grepstad, X-PEEM study of antiferromagnetic domain patterns in LaFeO₃ thin films and embedded nanostructures, *J. Electron Spectrosc. Relat. Phenomena* **185**, 381 (2012).

- [12] H. Meer, O. Gomonay, C. Schmitt, R. Ramos, L. Schnitzspahn, F. Kronast, M.-A. Mawass, S. Valencia, E. Saitoh, J. Sinova, L. Baldrati, and M. Kläui, Strain-induced shape anisotropy in antiferromagnetic structures, *Phys. Rev. B* **106**, 094430 (2022).
- [13] L. Baldrati, O. Gomonay, A. Ross, M. Filianina, R. Lebrun, R. Ramos, C. Leveille, F. Fuhrmann, T. R. Forrest, F. Maccherozzi, S. Valencia, F. Kronast, E. Saitoh, J. Sinova, and M. Kläui, Mechanism of Néel order switching in antiferromagnetic thin films revealed by magnetotransport and direct imaging, *Phys. Rev. Lett.* **123**, 177201 (2019).
- [14] S. Reimers, Y. Lytvynenko, Y. Niu, E. Golias, B. Sarpi, L. Ishibe-Veiga, T. Denneulin, A. Kovacs, R. Dunin-Borkowski, J. Bläßer, M. Kläui, and M. Jourdan, Current-driven writing process in antiferromagnetic Mn₂Au for memory applications, *Nat. Commun.* **14**, 1861 (2023).
- [15] J. Godinho, H. Reichlová, D. Kriegner, V. Novák, K. Olejník, Z. Kašpar, Z. Šobáň, P. Wadley, R. P. Campion, R. M. Otxoa, P. E. Roy, J. Železný, T. Jungwirth, and J. Wunderlich, Electrically induced and detected Néel vector reversal in a collinear antiferromagnet, *Nat. Commun.* **9**, 4686 (2018).
- [16] V. M. T. S. Barthem, C. V. Colin, H. Mayaffre, M. H. Julien, and D. Givord, Revealing the properties of Mn₂Au for antiferromagnetic spintronics, *Nat. Commun.* **4**, 2892 (2013).
- [17] P. Wadley *et al.*, Tetragonal phase of epitaxial room-temperature antiferromagnet CuMnAs, *Nat. Commun.* **4**, 2322 (2013).
- [18] S. P. Bommanaboyena, D. Backes, L. S. I. Veiga, S. S. Dhesi, Y. R. Niu, B. Sarpi, T. Denneulin, A. Kovács, T. Mashoff, O. Gomonay, J. Sinova, K. Everschor-Sitte, D. Schönke, R. M. Reeve, M. Kläui, H. J. Elmers, and M. Jourdan, Readout of an antiferromagnetic spintronics system by strong exchange coupling of Mn₂Au and Permalloy, *Nat. Commun.* **12**, 6539 (2021).
- [19] P. Wadley, V. Hills, M. R. Shahedkhah, K. W. Edmonds, R. P. Campion, V. Novak, B. Ouladdiaf, D. Khalyavin, S. Langridge, V. Saidl, P. Nemec, A. W. Rushforth, B. L. Gallagher, S. S. Dhesi, F. Maccherozzi, J. Zelezny, and T. Jungwirth, Antiferromagnetic structure in tetragonal CuMnAs thin films, *Sci. Rep.* **5**, 17079 (2015).
- [20] P. Wadley, K. W. Edmonds, M. R. Shahedkhah, R. P. Campion, B. L. Gallagher, J. Zelezny, J. Kunes, V. Novak, T. Jungwirth, V. Saidl, P. Nemec, F. Maccherozzi, and S. S. Dhesi, Control of antiferromagnetic spin axis orientation in bilayer Fe/CuMnAs films, *Sci. Rep.* **7**, 11147 (2017).
- [21] S. Y. Bodnar, M. Filianina, S. P. Bommanaboyena, T. Forrest, F. Maccherozzi, A. A. Sapozhnik, Y. Skourski, M. Kläui, and M. Jourdan, Imaging of current induced Néel vector switching in antiferromagnetic Mn₂Au, *Phys. Rev. B* **99**, 140409(R) (2019).
- [22] F. Krizek, Z. Kašpar, A. Vetuska, D. Kriegner, E. M. Fiordaliso, J. Michalicka, O. Man, J. Zubáč, M. Brajer, V. A. Hills, K. W. Edmonds, P. Wadley, R. P. Campion, K. Olejník, T. Jungwirth, and V. Novák, Molecular beam epitaxy of CuMnAs, *Phys. Rev. Mater.* **4**, 014409 (2020).
- [23] S. Reimers, D. Kriegner, O. Gomonay, D. Carbone, F. Krizek, V. Novak, R. P. Campion, F. Maccherozzi, A. Björlling, O. J. Amin, L. X. Barton, S. F. Poole, K. A. Omari, J. Michalicka, O. Man, J. Sinova, T. Jungwirth, P. Wadley, S. S. Dhesi, and K. W. Edmonds, Defect-driven antiferromagnetic domain walls in CuMnAs films, *Nat. Commun.* **13**, 724 (2022).
- [24] N. Hedrich, K. Wagner, O. V. Pylypovskiy, B. J. Shields, T. Kosub, D. D. Sheka, D. Makarov, and P. Maletinsky, Nanoscale mechanics of antiferromagnetic domain walls, *Nat. Phys.* **17**, 574 (2021).
- [25] A. Hubert and R. Schäfer, *Magnetic Domains: The Analysis of Magnetic Microstructures* (Springer, Heidelberg, 1998).
- [26] A. A. Sapozhnik, M. Filianina, S. Y. Bodnar, A. Lamirand, M.-A. Mawass, Y. Skourski, H.-J. Elmers, H. Zabel, M. Kläui, and M. Jourdan, Direct imaging of antiferromagnetic domains in Mn₂Au manipulated by high magnetic fields, *Phys. Rev. B* **97**, 134429 (2018).
- [27] K. Olejník, T. Seifert, Z. Kašpar, V. Novák, P. Wadley, R. P. Campion, M. Baumgartner, P. Gambardella, P. Nemec, J. Wunderlich, J. Sinova, P. Kuzel, M. Müller, T. Kampfrath, and T. Jungwirth, Terahertz electrical writing speed in an antiferromagnetic memory, *Sci. Adv.* **4**, eaar3566 (2018).
- [28] K. A. Omari, L. X. Barton, O. Amin, R. P. Campion, A. W. Rushforth, A. J. Kent, P. Wadley, and K. W. Edmonds, Low-energy switching of antiferromagnetic CuMnAs/GaP using sub-10 nanosecond current pulses, *J. Appl. Phys.* **19**, 193906 (2020).
- [29] M. Wang *et al.*, Spin flop and crystalline anisotropic magnetoresistance in CuMnAs, *Phys. Rev. B* **101**, 094429 (2020).
- [30] H. Jani, J.-C. Lin, J. Chen, J. Harrison, F. Maccherozzi, J. Schad, S. Prakash, C.-B. Eom, A. Ariando, T. Venkatesan, and P. G. Radaelli, Antiferromagnetic half-skyrmions and bimerons at room temperature, *Nature* **590**, 74 (2021).
- [31] O. J. Amin, S. F. Poole, S. Reimers, L. X. Barton, F. Maccherozzi, S. S. Dhesi, V. Novák, F. Krizek, J. S. Chauhan, R. P. Campion, A. W. Rushforth, T. Jungwirth, O. A. Tretiakov, K. W. Edmonds, and P. Wadley, Antiferromagnetic half-skyrmions electrically generated and controlled at room temperature, *Nat. Nanotech.* **18**, 849 (2023).
- [32] M. Jourdan, H. Bräuning, A. Sapozhnik, H. Elmers, H. Zabel, and M. Kläui, Epitaxial Mn₂Au thin films for antiferromagnetic spintronics, *J. Phys. D: Appl. Phys.* **48**, 385001 (2015).
- [33] A. A. Sapozhnik, R. Abrudan, Y. Skourski, M. Jourdan, H. Zabel, M. Kläui, and H.-J. Elmers, Manipulation of antiferromagnetic domain distribution in Mn₂Au by ultrahigh magnetic fields and by strain, *PSS (RRL)* **11**, 1600438 (2017).
- [34] See the Supplemental Material at <http://link.aps.org/supplemental/10.1103/PhysRevApplied.21.064030> for the domain-wall width-fitting protocol.
- [35] A. Wittmann *et al.*, Role of substrate clamping on anisotropy and domain structure in the canted antiferromagnet α -Fe₂O₃, *Phys. Rev. B* **106**, 224419 (2022).
- [36] L. Daniel, O. Hubert, N. Buiron, and R. Billardon, Reversible magneto-elastic behavior: A multiscale approach, *J. Mech. Phys. Solids* **56**, 1018 (2008).
- [37] A. DeSimone and R. D. James, A constrained theory of magnetoelasticity, *J. Mech. Phys. Solids* **50**, 283 (2002).